Large, Tunable Valley Splitting and Single-Spin Relaxation Mechanisms in a Si/Si$_x$Ge$_{1-x}$ Quantum Dot

Arne Hollmann,[1] Tom Struck,[1] Veit Langrock,[1] Andreas Schmidbauer,[2] Floyd Schauer,[2] Tim Leonhardt,[1] Kentarou Sawano,[3] Helge Riemann,[4] Nikolay V. Abrosimov,[4] Dominique Bougeard,[2] and Lars R. Schreiber ®[1,*]

[1]*JARA-FIT Institute for Quantum Information, Forschungszentrum Jülich GmbH and RWTH Aachen University, Aachen, Germany*
[2]*Institut für Experimentelle und Angewandte Physik, Universität Regensburg, Regensburg, Germany*
[3]*Advanced Research Laboratories, Tokyo City University, Tokyo, Japan*
[4]*Leibniz-Institut für Kristallzüchtung (IKZ), Berlin, Germany*

Valley splitting is a key feature of silicon-based spin qubits. Quantum dots in Si/Si$_x$Ge$_{1-x}$ heterostructures reportedly suffer from a relatively low valley splitting, limiting the operation temperature and the scalability of such qubit devices. Here, we demonstrate a robust and large valley splitting exceeding 200 μeV in a gate-defined single quantum dot, hosted in molecular-beam-epitaxy-grown ^{28}Si/Si$_x$Ge$_{1-x}$. The valley splitting is monotonically and reproducibly tunable up to 15% by gate voltages, originating from a 6-nm lateral displacement of the quantum dot. We observe static spin relaxation times $T_1 > 1$ s at low magnetic fields in our device containing an integrated nanomagnet. At higher magnetic fields, T_1 is limited by the valley hotspot and by phonon noise coupling to intrinsic and artificial spin-orbit coupling, including phonon bottlenecking.

I. INTRODUCTION

Silicon has proven to be an excellent host material for spin qubits [1]. Demonstrated fidelities of single-qubit gates higher than 99.9% [2–5] are beyond the error correction threshold [6] and the fidelity of two-qubit gates is steadily increasing [7–9]. Nuclear purification [10], which reduces spin dephasing induced by hyperfine coupling, rendered this progress possible. Applying industrial fabrication processes and integrating conventional silicon electronics open up the perspective of a highly scalable and dense quantum computing architecture [11–13]. In particular, electrons trapped in electrostatically defined quantum dots (QDs) in Si/Si$_x$Ge$_{1-x}$ stand out by the excellent control of both the QD energies and the tunnel barriers [14,15], both of which are important for universal multiqubit manipulation. The Si$_x$Ge$_{1-x}$ barrier layer separates charged defects at the gate dielectric oxide interface [14,16] from the qubits in the silicon quantum well (QW) and thus reduces qubit dephasing due to charge noise. The major challenge for scaling up in this material system is its difficult-to-control and reportedly small valley splitting E_{VS}, mainly below 70 μeV [8,17–25]. The excited valley

state may then be occupied either by thermal excitation [19,26] or by fast spin relaxation [27], severely hampering the qubit control. E_{VS} is known to crucially depend on the atomistic details at the Si/Si$_x$Ge$_{1-x}$ interface as well as on an applied out-of-plane electric field [18,27–32]. A large E_{VS} compared to the electron temperature and the Zeeman energy is thus highly desired to harness the full potential of Si/Si$_x$Ge$_{1-x}$ as one of the most promising hosts for spin qubits.

In this work, we present a singly charged gate-defined quantum dot with an integrated nanomagnet [33] in a molecular beam epitaxy (MBE)-grown ^{28}Si/Si$_x$Ge$_{1-x}$ heterostructure, revealing a remarkably high valley splitting E_{VS} beyond 200 μeV. The energy values extracted both from pulsed gate spectroscopy and from the magneto-dependence of the spin relaxation time T_1 [34] are consistent. We find this valley splitting to be robust against lateral displacements of the QD, experimentally realized by adjusting the dot-defining gate voltages while maintaining constant the dot size and orbital energy. The QD characteristics, including E_{VS}, are reproducible for continuous displacements of the QD and also for more abrupt switching between QD positions, indicating that this single-electron dot is not limited by potential disorder. We demonstrate a monotonic tunability of E_{VS} of at

*lars.schreiber@physik.rwth-aachen.de

least 15% to result from a gate-controlled and reproducible displacement of the QD relative to ^{28}Si/Si$_x$Ge$_{1-x}$ interface steps [35]. Analyzing the magneto-dependence of the spin relaxation time T_1, which reaches values beyond 1 s, we find consistent results for a few QD positions regarding the relaxation mechanisms acting at the prominent spin-valley-dominated T_1 hotspot as well as in the lower- and higher-energy regions [25,34,36,37].

II. DEVICE STRUCTURE AND SETUP

Our double quantum dot (DQD) device with an integrated nanomagnet (Fig. 1) confines electrons in an undoped ^{28}Si QW with 60 ppm of residual ^{29}Si. The heterostructure is fabricated by solid-source MBE. A relaxed virtual substrate consists of a graded buffer grown at 500 °C up to a composition of Si$_{0.7}$Ge$_{0.3}$ on a Si substrate without intentional miscut and a layer of constant-composition Si$_{0.7}$Ge$_{0.3}$. It provides the basis for a 12-nm ^{28}Si QW grown using a source material of isotopically purified ^{28}Si with 60 ppm of remaining ^{29}Si with a rate of 0.14 Å/s at a substrate temperature of 350 °C. The QW is separated from the interface by 45-nm Si$_{0.7}$Ge$_{0.3}$. The structure is protected by a 1.5-nm naturally oxidized Si cap [see Fig. 1(a)]. The implanted ohmic contacts to the QW are thermally activated by a rapid anneal at 700 °C. The mobility of the 2DEG formed in the QW, as obtained by Hall measurements at a temperature of 1.5 K, is of the order of 55 000 cm^2/(V s) at an electron density of 6×10^{11} cm^{-2} and is limited by remote impurity scattering [10].

A 20-nm layer of Al$_2$O$_3$ grown by atomic layer deposition insulates the depletion gate layer depicted in Fig. 1(b) and the underlying heterostructure. The depletion gates are fabricated by means of electron beam lithography. A Co nanomagnet, colored in blue in Fig. 1(b), is added to the depletion gate layer in order to provide a local magnetic field gradient for electric dipole spin resonance. A second gate layer, insulated from the depletion gates by 80 nm of Al$_2$O$_3$, is used to induce a two-dimensional electron gas in the QW via the field effect and provide reservoirs for the dot-defining and charge-sensing parts of the device. A scanning electron micrograph of the second gate layer is shown in Fig. 1 within the Supplemental Material [38]. A single-electron transistor (SET) for charge detection is formed on the right-hand side of the device between reservoirs III and IV [colored in red in Fig. 1(b)]. The device is measured in an Oxford Triton dilution refrigerator at a base temperature of 40 mK and electron temperature of 114 mK. All dc lines are heavily filtered using pi filters at room temperature followed by copper-powder filters and a second-order RC low-pass filter at base temperature (see Note 1 within the Supplemental Material [38] for details).

III. RESULTS

We tune the DQD to the single-electron regime as illustrated in the charge stability diagram in Fig. 1(c), where (N_L, N_R) denotes the electron occupancy in the left and right QD, respectively. In the following, the device is operated across the (0,0)-(1,0) charge transition far away from the (1,0)-(1,1) transition. An in-plane external magnetic field B_{ext} is applied along the long axis of the nanomagnet
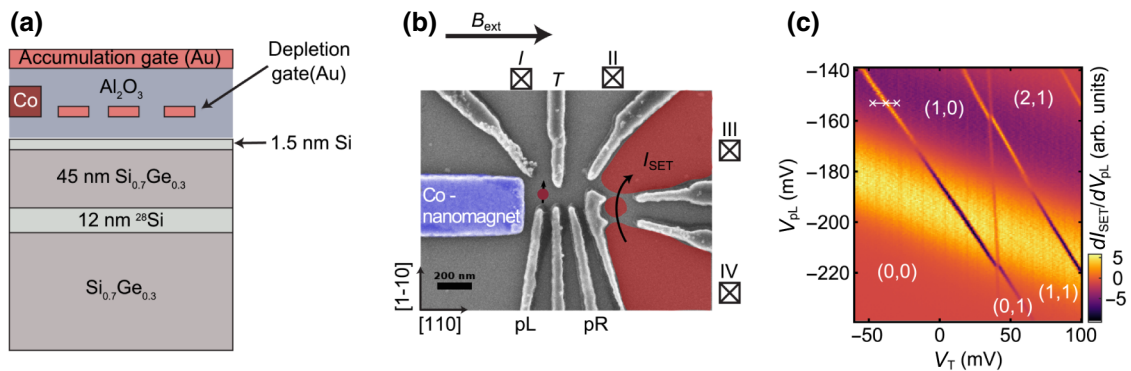

FIG. 1. ^{28}Si/Si$_x$Ge$_{1-x}$ device and charge stability diagram. (a) Schematic cross section of the layer structure of the device. A 12-nm purified ^{28}Si quantum well (with 60 ppm of ^{29}Si) is grown on a Si$_{0.7}$Ge$_{0.3}$ virtual substrate. Electrostatic depletion gates (Au) are separated by 20-nm Al$_2$O$_3$. A cobalt nanomagnet is added in this gate layer. (b) Top view: scanning electron image of the depletion gate layout of our DQD device with integrated nanomagnet and charge sensor. The global accumulation gate that is located in a different layer (see Note 1 within the Supplemental Material [38]) is not resolved here. The electron reservoirs are labeled by squares and roman numerals. The cobalt nanomagnet indicated in blue introduces a magnetic field gradient and at the same time acts as an electrostatic confining gate. Crystallographic axes are indicated at the bottom left. The single-electron transistor formed on the right of the device for integrated charge sensing of the occupation of the QD is colored in red. (c) Charge stability diagram of the DQD device close to the single-electron regime. The single-electron quantum dot (1,0) is solely tunnel-coupled to the reservoir I. Unload, load, and readout positions in pulsed operation are marked by white crosses.

as sketched in Fig. 1(b). The stray field of the nanomagnet adds an additional longitudinal field component of $B_0 = 40.71$ mT at the left QD position, as shown in Note 2 within the Supplemental Material [38].

A. Measurement of the orbital and valley splitting

As a first characterization of the device, we perform pulsed gate spectroscopy at the (0,0)-(1,0) charge transition. A 50% duty-cycle square pulse with amplitude V_{pulse} is added to the dc voltage of the gate pR indicated in Fig. 1(b) (see Note 3 within the Supplemental Material [38]). As soon as V_{pulse} is high enough to load an electron into an excited state, the effective loading rate increases: the average dot occupation and with it the average sensor current I_{SET} change. To clearly separate the spin states of this dot configuration, we fix the external magnetic field to 3 T. The visibility of each transition depends on the ratio of the tunnel rate into the corresponding excited state and the frequency of the square pulse. All four spin-valley states $(|\downarrow -\rangle, |\downarrow +\rangle, |\uparrow -\rangle, |\uparrow +\rangle)$ and the excited orbital state are clearly resolved in Fig. 2(a). The orbital spin states are well separated from the lower-lying spin-valley states. Using the applied Zeeman energy to determine the lever arm $\alpha = 0.06$ eV/V of gate pR, we calibrate the pR voltage to the change of chemical potential of the QD. This allows us to extract an orbital splitting of $E_{orb} = \alpha V_{orb} = 1.45$ meV, defining a large window for the operation of spin qubits in the valley states. There, whenever the valley splitting E_{VS} is of the order of the Zeeman splitting E_Z, spin-valley mixing becomes the dominant decay channel [34], the spin relaxation time T_1 then being ultimately limited by the inter-valley transition decay for $E_{VS} = E_Z$. In contrast to strongly confined electrons in MOS quantum dots [27,39,40], this effect can hamper Pauli spin blockade readout and operation at elevated temperature, thus affecting the scalability of Si/Si$_x$Ge$_{1-x}$ [26]. Here, from pulsed gate spectroscopy, based on the lever arm, we estimate the valley splitting in our device to be extremely large with $E_{VS} \approx 226$ μeV (two to three times larger than most of the reported values [8,19–23,25]), motivating a more precise quantification of this valley splitting in the following.

To do so, we measure the spin relaxation rate in a large range of externally applied magnetic fields, allowing us to realize the condition $E_{VS} = E_Z$, where a peak (hotspot) in the spin relaxation is expected [25,34] due to spin-valley mixing. The position of this distinct and sharp peak of the spin relaxation spectrum allows a precise measure of E_{VS}. Compared to the pulsed gate spectroscopy experiments, we reduce the tunnel coupling to the reservoir to 5 ms, in order to perform single-shot spin detection using energy-selective tunneling to the reservoir [41]. This slightly reduces the QD size, leading to an increased orbital energy as will be discussed in the next section. We enhance
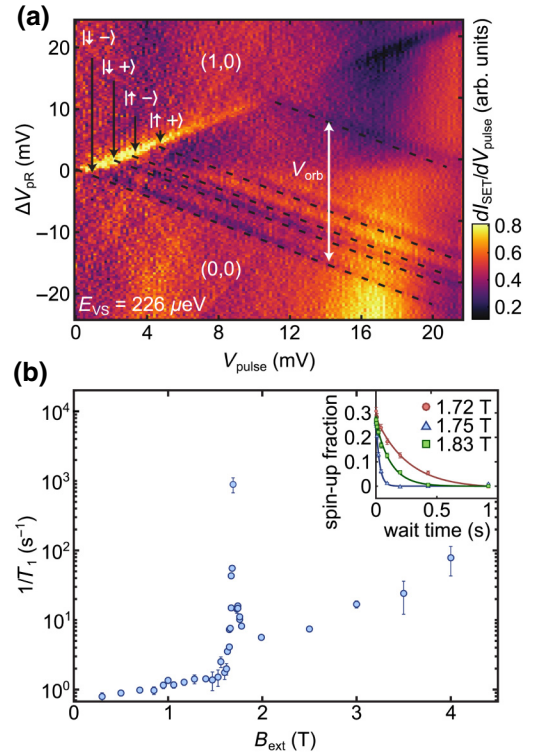

FIG. 2. Pulsed gate spectroscopy and spin relaxation measurement. (a) Pulsed gate spectroscopy on gate pR at an external magnetic field of 3 T. We use the gate pR as it has a low cross-coupling to the reservoir tunnel barrier. The time-averaged current change dI_{SET}/dV_{pulse} is plotted as a function of the dc voltage offset ΔV_{pR} and the square pulse amplitude V_{pulse}, both applied to the gate pR. We chose ΔV_{pR} to be zero at the (0,0)-(0,1) dot-occupation transition. The plotted SET current is the sum of the SET currents from two measurements recorded at a pulse frequency of 10 and 50 kHz, respectively. White labels mark the occupation of excited spin $(|\downarrow\rangle, |\uparrow\rangle)$, valley $(|-\rangle, |+\rangle)$, and orbital states. (b) Spin relaxation rate $1/T_1$ as a function of the external magnetic field B_{ext}. At $B \sim 2$T, we observe a steep rise in the spin relaxation (hotspot). Inset: spin-up fraction as a function of the wait time for three magnetic field configurations in close proximity to the hotspot. The voltage tuning of the QD in (b) slightly differs from the configuration in (a).

the QD loading rate (see Note 4 within the Supplemental Material [38]) by using the gate T shown in Fig. 1(c). We pulse the voltage of this gate to load and unload an electron between reservoir I and the left QD. We observe single exponential decays of the measured spin-up fraction as a function of the duration of the load pulse, as exemplarily shown in the inset of Fig. 2(b) for three magnetic field values. The spin relaxation rate $1/T_1$ is extracted from these decays and plotted as a function of B_{ext} in the main graph of Fig. 2(b). The low magnetic field range, relevant for spin qubit operation ($B_{ext} \sim 0.7$ T for 20 GHz electron spin resonance), yields long relaxation times $T_1 > 1$ s that are rather insensitive to B_{ext}. We will address this regime

together with the high-field range in a later section and firstly concentrate on the sharp relaxation peak at $B_{\text{ext}} = 1.69$ T, which corresponds to the realization of $E_{\text{VS}} = E_Z$. Taking the longitudinal magnetic field offset (40.71 mT) of the nanomagnet at the QD position into account, the magnetic field position of this hotspot confirms the valley splitting in our device to be remarkably high, yielding a value of $E_{\text{VS}} = 201\ \mu$eV. Given the spin-selective nature of our readout, a variation of the amplitude of the loading pulse discussed in Note 5 within the Supplemental Material [38] validates our assignment of the spin states shown in Fig. 2(a) and $E_{\text{VS}} = 201\ \mu$eV. We also exclude a valley splitting smaller than the thermal energy, since we observe a clear single-transition chevron pattern (see Note 6 within the Supplemental Material [38]).

The energy splitting E_{VS} between the two valley states is predicted to mainly depend on two parameters in $\text{Si}/\text{Si}_x\text{Ge}_{1-x}$: the applied out-of-plane electric field E_z and the sharpness of the QW interface [28,29,31,32]. In particular, an overlap of the electron wavefunction with atomic steps formed at this interface during the epitaxy of the heterostructure will reduce the valley splitting. Therefore, measuring a higher E_{VS} for comparable electric field values E_z may be a consequence of either a sharp QW interface or a small overlap, for example because of a strong lateral QD confinement. The latter may originate from potential disorder induced by bulk defects or defects at the oxide interface. Such defects will localize the QD uncontrollably. Note that the observed $E_{\text{orb}} = 1.45$ meV [see Fig. 2(a)] in our device points towards a QD potential that is formed by the potential of the gates. Assuming a lateral harmonic potential and taking the radius of the dot to be half of the full width at half maximum of the ground state, the corresponding QD has a radius of approximately 19 nm. It thus overlaps with a large QW interface area (comparable to, e.g., Ref. [14], while in Ref. [17] a high E_{VS} due to an unconventional small QD has been reported) and may thus indicate advantageous QW interface characteristics with regard to E_{VS}. The $^{28}\text{Si}/\text{Si}_x\text{Ge}_{1-x}$ heterostructure used here (see Sec. II) is grown by solid-source MBE. The substrate temperature of $350\,^\circ$C in conjunction with adapted growth rates and the solid-source purity [10] may be comparatively beneficial for achieving sharp interfaces. In order to evaluate the role of the out-of-plane electric field E_z and to further exclude potential disorder as the reason for the observed high E_{VS}, we test in the following the evolution of E_{VS} when varying the dot-defining gate voltages.

B. Tuning the valley splitting

We systematically vary the voltages on both gates pL and T in steps of 20 mV, which keeps the chemical potential of the QD and the tunnel rate to the reservoir constant. For each voltage step, we measure the relaxation spectrum
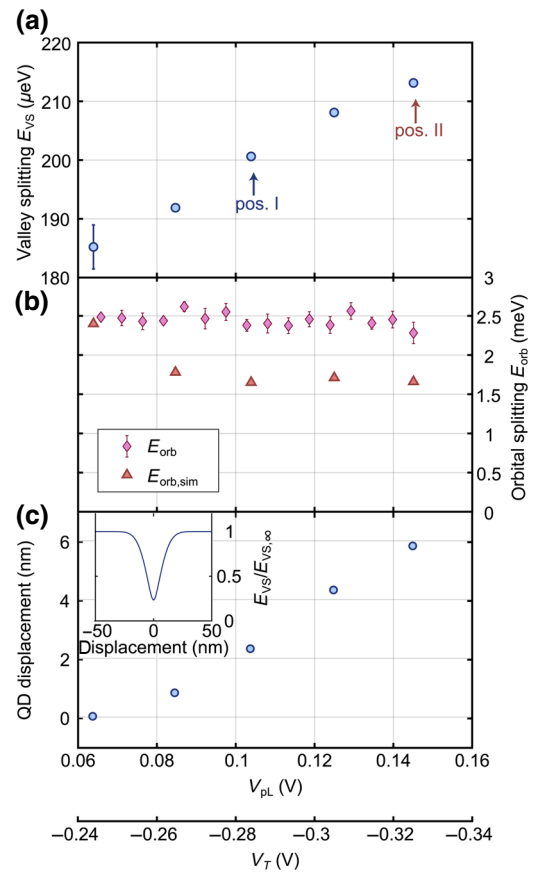

FIG. 3. Control of the valley splitting. (a) Valley splitting E_{VS} for different QD configurations defined by the voltages on pL and T. E_{VS} is extracted from the relaxation hotspot. The two labeled positions I and II correspond to the configurations used to analyze the spin relaxation mechanism in Fig. 4. (b) Orbital splitting E_{orb} extracted from pulsed gate spectroscopy measurements. $E_{\text{orb,sim}}$ indicates simulation results from a realistic Schrödinger-Poisson simulation of the single-electron QD (see Note 7 within the Supplemental Material [38]). (c) Simulated dot displacement for the given pL and T voltage configurations. Inset: calculated change of valley splitting $E_{\text{VS}}/E_{\text{VS},\infty}$ for a QD displacement across a single atomic step placed at 0 nm.

as a function of magnetic field in close proximity to the spin relaxation hotspot. The resulting E_{VS} is depicted in Fig. 3(a) as a function of the pL-T voltage configuration. The values of E_{VS} remain remarkably high at the different gate voltages. All configurations are found to be robust and reproducible: the respective E_{VS} values are also stable when jumping between different voltage configurations instead of steadily changing the voltages. Notably, we can monotonically tune E_{VS} with pL and T: changing the gate voltages in a range of 80 mV, E_{VS} monotonically changes by 28 μeV, corresponding to a tuning range of 15%. Dependence of the singlet-triplet splitting on lateral QD displacement was observed by magnetospectroscopy in Ref. [18].

To verify the impact of the gate voltage tuning on the lateral confinement potential of our single-electron QD, we measure the orbital splitting E_{orb} by pulsed gate spectroscopy for all the voltage configurations shown in Fig. 3(b): we find $E_{orb,exp}$ to remain unchanged at approximately 2.5 meV. This trend of an orbital splitting unaffected by the gate voltage tuning is confirmed in a realistic Schrödinger-Poisson simulation of the single-electron QD that we subject to the same gate voltage tuning range. As shown in Fig. 3(b), $E_{orb,sim}$ is also unchanged across this tuning range. Concomitantly, the in-plane shape of the QD remains constant in the simulation (see Note 7 within the Supplemental Material [38]). We thus conclude that the in-plane confinement and size of our QD are conserved during the operated gate voltage variations. Note that we intentionally increase the tunnel coupling to the reservoir for the pulsed gate spectroscopy shown in Fig. 2(a) by increasing the size of the QD. Thus, we use a gate voltage configuration that is not covered by the configurations shown in Fig. 3, but still we observe a 25-μeV larger valley splitting compared to the hotspot in Fig. 2(b). This suggests a robust and tunable valley splitting in an even larger gate voltage parameter space.

The impact of the out-of-plane electric field E_z on the value of the valley splitting E_{VS} in silicon qubit devices [29,31,35,42] is particularly visible for MOS-based devices where the electron is strongly confined to the Si/SiO$_2$ interface. In such devices, a tunable valley splitting that depends linearly on E_z for strong fields has been observed [27]. Here, for our device, however, we find a comparatively weak value of the out-of-plane electric field E_z in our simulation. E_z also shows no significant variation between the different tested gate voltage configurations. In fact, as shown in Fig. 3(c), the main effect of our voltage tuning is a monotonic 6-nm in-plane displacement of the QD over the full conducted pL and T voltage range, according to the simulation. Noting the monotonic evolution of E_{VS} when continuously adjusting the gate voltages on the one hand, combined with the observation of an excellent reproducibility of high E_{VS} when more abruptly switching between the different gate voltage configurations on the other hand, we conclude that our device is not limited by potential disorder in the single-electron regime. Instead, our results strongly indicate that we can robustly and significantly displace the QD in the ^{28}Si QW plane and that the valley splitting does not show abrupt disorder-induced variations on short lateral length scales.

Regarding the continuous variation of up to 15% for E_{VS} for the tested gate voltage configurations, we believe that it results from the controlled displacement relatively to atomic steps at the ^{28}Si/Si$_x$Ge$_{1-x}$ interface. We calculate the change in valley splitting induced by an atomic step analytically, as shown in the inset of Fig. 3(c). A single interface step leads to a valley phase of $\theta = 2k_0 \times a_{Si}/4 = 0.85\pi$, where $a_{Si}/4$ is the height of a mono-atomic layer in

silicon and $k_0 = 2\pi/a_{Si} \times 0.85$ is the position of the valley minimum along the Δ direction. As can be seen in the inset of Fig. 3(c), in the vicinity of an atomic step (placed at 0 nm), E_{VS} changes by several tens of percent within a few nanometers, dropping down to $E_{VS,\infty} \cos(\theta/2)$, where $E_{VS,\infty}$ is the valley splitting far away from the interface step.

C. Spin relaxation mechanisms

Having analyzed the high and robust valley splitting in our device, which manifests through the prominent spin relaxation hotspot in Fig. 2(b), we now discuss the magnetic field dependence of the spin relaxation time T_1 in more detail. The three main features of this dependence shown in Fig. 2(b) are the sharp valley mixing hotspot, a strong B_{ext} dependence in the field regime beyond the hotspot, and a roughly magnetic field-independent T_1 in the low-field regime. We fit these magnetic field dependencies for two gate voltage configurations of the device in a large range of magnetic fields (configurations I and II, marked in Fig. 3). The fitting formula is based on a rate equation including spin-valley (SV) and both intrinsic and artificial spin-orbit (SO) coupling, the latter of which is given by the simulated gradient magnetic field of the nanomagnet. These coupling mechanisms are combined with Johnson noise (J) and phonon noise (ph), respectively [25,34,37]:

$$\Gamma_{tot} = \Gamma_{SV,J} + \Gamma_{SO,J} + \Gamma_{SV,ph} + \Gamma_{SO,ph}. \quad (1)$$

Our approach to the rate equation and the extracted fit parameters for two different QD positions are discussed in more detail in Note 8 within the Supplemental Material [38]. The colored solid lines in Fig. 4 represent the different spin relaxation contributions Γ_i of Eq. (1) in both gate configurations, allowing us to analyze the contributions of the relevant relaxation mechanisms to the different magnetic field regions. The prominent spin relaxation hotspot is in excellent agreement with a fit dominated by SV combined with both phonon and Johnson noise ($\Gamma_{SV,J} + \Gamma_{SV,ph}$). From the peak width we determine a value of the product Δr^{+-} of ≈ 15.1 neV nm for the configuration in Fig. 4(a), where Δ and r^{+-} are the spin-valley coupling energy and the valley-orbit dipole strength, respectively. In Note 8 within the Supplemental Material [38], we also evaluate the peak width that would result if the hotspot was of orbital nature: we find a significantly larger value than the one extracted from Fig. 4 in both dot configurations, strongly supporting our attribution of the spin relaxation hotspots to the spin-valley coupling.

The rate equation suggests the magnetic field range beyond the hotspot to be governed by SO and phonon noise. The intrinsic and artificial SO interactions contribute with magnetic field dependencies of $(B_{ext})^7$ and $(B_{ext})^5$, respectively. In Fig. 4, we find the best fit agreement when combining both dependencies with a phonon bottleneck
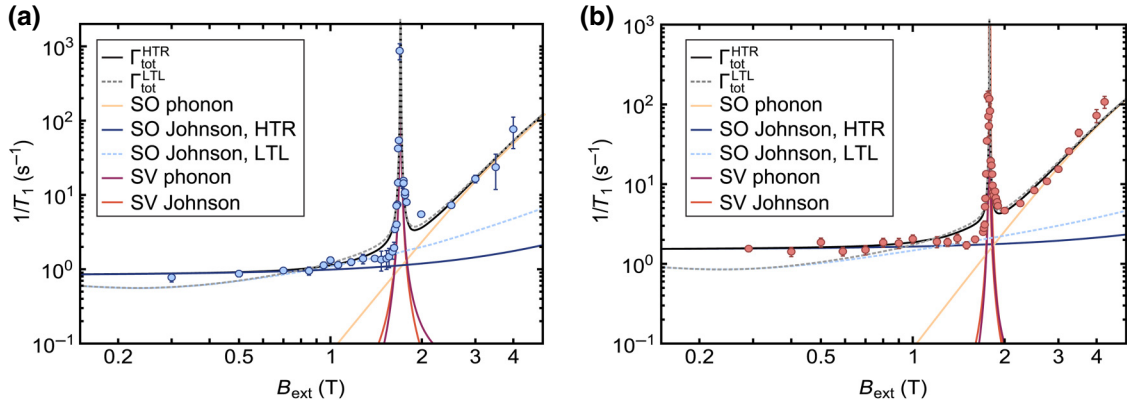
FIG. 4. Spin relaxation rate fitted with rate equation. (a),(b) correspond to positions I and II, respectively, as labeled in Fig. 3. $\Gamma_{\text{tot}}^{\text{HTR}}$ corresponds to the elevated temperature resistor model and $\Gamma_{\text{tot}}^{\text{LTL}}$ to the lossy transmission line model, labeled by the solid black and gray dashed lines, respectively (see main text and Note 8 within the Supplemental Material [38]). The different single relaxation contributions are indicated by the colored lines.

for coupling to a QD [36,43]. The bottleneck effect gets relevant beyond 2.4 T, corresponding to approximately 67 GHz, the point where the inverse of the phonon wave number exceeds the QD size.

In the low-field regime, we observe a remarkably long spin relaxation rate ($T_1 > 1$ s) [Fig. 4(a)], which is nearly independent of B_{ext}. This saturation may appear also in Ref. [25], however, overlayed by the low-energy side of the valley relaxation hotspot, due to a lower E_{VS} in the devices discussed there. We consider two mechanisms as possible sources for the experimentally observed trend. Firstly, capacitively coupling artificial SO combined with white electric noise [e.g., Johnson noise from a high-temperature resistor (HTR) at a temperature above 2.5 K] to the QD will result in a B_{ext}-independent spin relaxation. However, as shown in Note 8 within the Supplemental Material [38], we find the magnitude of the fitted Johnson noise (blue solid line in Fig. 4) to be much larger than the actual resistor values at elevated temperature in our setup, the high-frequency Johnson noise of which is attenuated by copper-powder filters and high-frequency attenuators, respectively. Given this discrepancy with the characteristics of our setup, we find this mechanism solely inducing our observed T_1 trend unlikely, although the fit shown by the solid black line in Fig. 4 may look reasonable.

A second candidate for inducing Johnson noise into the device are fluctuations in the electron reservoir coupled to the QD. As discussed in more detail in Note 8 within the Supplemental Material [38], we therefore consider the ohmic contact resistances and resistances of the Si/Si$_x$Ge$_{1-x}$ 2DEG to form a lossy transmission line (LTL) together with the global inducing gate (blue dashed line in Fig. 4). A spin relaxation that includes this type of Johnson noise on the electron reservoirs combined with $\Gamma_{\text{SV},J} + \Gamma_{\text{SV,ph}} + \Gamma_{\text{SO,ph}}$ is plotted as the gray dashed line in Fig. 4 ($\Gamma_{\text{tot}}^{\text{LTL}}$). Although the fit may look reasonable for the gate

voltage configuration in Fig. 4(a), we find it to be in less good agreement with the other tested QD position where the low-field regime is clearly independent of the magnetic field [Fig. 4(b)]. The black line shown in Fig. 4 ($\Gamma_{\text{tot}}^{\text{HTR}}$) depicts the total fit $\Gamma_{\text{tot}}(B_{\text{ext}})$ to the measured spin relaxation rate, combining the dominant relaxation mechanisms for each magnetic field region for this exemplary gate configuration. All in all, we find an excellent agreement for all tested dot positions for the sharp hotspot peak and the high-field region, while more statistics and a higher magnetic field resolution of the low-field region seem to be required to unambiguously identify the dominant noise source.

IV. DISCUSSION

In conclusion, we characterize a single-electron spin qubit in MBE-grown isotopically purified ^{28}Si/Si$_x$Ge$_{1-x}$ with pulsed gate spectroscopy and through its magneto-dependence of the spin relaxation time T_1. The dot-defining gate layout allows us to laterally displace this QD (radius of approximately 19 nm) by changing the gate voltages while keeping its size and orbital energy $E_{\text{orb,exp}}$ constant. We find consistently high valley splittings $E_{\text{VS}} \sim 200$ μeV and a well-separated $E_{\text{orb,exp}}$, both when continuously sweeping gate voltages between different QD positions and also when more abruptly switching between QD positions. The robustness and reproducibility of the QD characteristics with the dot displacement as well as our simulation of the out-of-plane electric field E_z strongly indicate that our QD is not dominated by potential disorder and that the consistently high value of E_{VS} does not result from disorder confinement or E_z, but seems to be due to ^{28}Si/Si$_x$Ge$_{1-x}$ QW interfaces that are advantageous in terms of E_{VS}, albeit the heterostructure undergoes an implantation anneal at 700 °C. One reason for these findings may be the comparatively low substrate temperatures used in MBE. The monotonic variation of

E_{VS} of 15% that we observe experimentally is attributed to a reproducible and gate-controlled displacement relative to atomic steps at the QW interface. This robust displacement process supports our conclusion of dealing with a comparatively smooth (i.e., free from short-length-scale disorder) $^{28}Si/Si_xGe_{1-x}$ interface for this device. The closer analysis of the magneto-dependence of the relaxation time T_1 confirms the prominent relaxation hotspot to be dominated by spin-valley coupling, combined with Johnson and phonon noise. At lower magnetic fields, the relaxation times $T_1 > 1$ s are relatively insensitive to the external magnetic field. At higher fields, we find very good agreement for fits that include phonon noise acting with a combination of intrinsic and artificial spin-orbit coupling, in the presence of phonon bottlenecking. The observed artificial spin-orbit coupling is fully consistent with the field gradient induced by the nanomagnet that is integrated into the dot-defining gate layout. The demonstration of consistently high E_{VS} and the absence of short-length-scale disorder in this device provides a promising perspective towards higher-yield spin qubit devices in Si/Si_xGe_{1-x} QDs.

ACKNOWLEDGMENTS

[1] F. A. Zwanenburg, A. S. Dzurak, A. Morello, M. Y. Simmons, L. C. L. Hollenberg, G. Klimeck, S. Rogge, S. N. Coppersmith, and M. A. Eriksson, Silicon quantum electronics, Rev. Mod. Phys. **85**, 961 (2013).

[2] M. Veldhorst, J. C. C. Hwang, C. H. Yang, A. W. Leenstra, B. de Ronde, J. P. Dehollain, J. T. Muhonen, F. E. Hudson, K. M. Itoh, A. Morello, and A. S. Dzurak, An addressable quantum dot qubit with fault-tolerant control-fidelity, Nat. Nanotechnol. **9**, 981 (2014).

[3] A. Laucht, J. T. Muhonen, F. A. Mohiyaddin, R. Kalra, J. P. Dehollain, S. Freer, F. E. Hudson, M. Veldhorst, R. Rahman, G. Klimeck, K. M. Itoh, D. N. Jamieson, J. C. McCallum, A. S. Dzurak, and A. Morello, Electrically controlling single-spin qubits in a continuous microwave field, Sci. Adv. **1**, e1500022 (2015).

[4] J. T. Muhonen, A. Laucht, S. Simmons, J. P. Dehollain, R. Kalra, F. E. Hudson, S. Freer, K. M. Itoh, D. N. Jamieson, J. C. McCallum, A. S. Dzurak, and A. Morello, Quantifying the quantum gate fidelity of single-atom spin qubits in silicon by randomized benchmarking, J. Phys.: Condens. Matter **27**, 154205 (2015).

[5] J. Yoneda, K. Takeda, T. Otsuka, T. Nakajima, M. R. Delbecq, G. Allison, T. Honda, T. Kodera, S. Oda, Y. Hoshi, N. Usami, K. M. Itoh, and S. Tarucha, A quantum-dot spin qubit with coherence limited by charge noise and fidelity higher than 99.9%, Nat. Nanotechnol. **13**, 102 (2017).

[6] A. G. Fowler, M. Mariantoni, J. M. Martinis, and A. N. Cleland, Surface codes: Towards practical large-scale quantum computation, Phys. Rev. A **86**, 032324 (2012).

[7] M. Veldhorst, C. H. Yang, J. C. Hwang, W. Huang, J. P. Dehollain, J. T. Muhonen, S. Simmons, A. Laucht, F. E. Hudson, K. M. Itoh, A. Morello, and A. S. Dzurak, A two-qubit logic gate in silicon, Nature **526**, 410 (2015).

[8] T. F. Watson, S. G. J. Philips, E. Kawakami, D. R. Ward, P. Scarlino, M. Veldhorst, D. E. Savage, M. G. Lagally, M. Friesen, S. N. Coppersmith, M. A. Eriksson, and L. M. K. Vandersypen, A programmable two-qubit quantum processor in silicon, Nature **555**, 633 (2017).

[9] W. Huang, C. H. Yang, K. W. Chan, T. Tanttu, B. Hensen, R. C. C. Leon, M. A. Fogarty, J. C. C. Hwang, F. E. Hudson, K. M. Itoh, A. Morello, A. Laucht, and A. S. Dzurak, Fidelity benchmarks for two-qubit gates in silicon, Nature **569**, 532 (2019).

[10] A. Wild, J. Kierig, J. Sailer, J. W. Ager, E. E. Haller, G. Abstreiter, S. Ludwig, and D. Bougeard, Few electron double quantum dot in an isotopically purified ^{28}Si quantum well, Appl. Phys. Lett. **100**, 143110 (2012).

[11] C. D. Hill, E. Peretz, S. J. Hile, M. G. House, M. Fuechsle, S. Rogge, M. Y. Simmons, and L. C. L. Hollenberg, A surface code quantum computer in silicon, Sci. Adv. **1**, e1500707 (2015).

[12] J. O'Gorman, N. H. Nickerson, P. Ross, J. J. Morton, and S. C. Benjamin, A silicon-based surface code quantum computer, npj Quantum Inf. **2**, 15019 (2016).

[13] M. Veldhorst, H. G. Eenink, C. H. Yang, and A. S. Dzurak, Silicon CMOS architecture for a spin-based quantum computer, Nat. Commun. **8**, 1766 (2017).

[14] D. M. Zajac, T. M. Hazard, X. Mi, E. Nielsen, and J. R. Petta, Scalable Gate Architecture for a One-Dimensional Array of Semiconductor Spin Qubits, Phys. Rev. Appl. **6**, 054013 (2016).

[15] A. R. Mills, D. M. Zajac, M. J. Gullans, F. J. Schupp, T. M. Hazard, and J. R. Petta, Shuttling a single charge across a one-dimensional array of silicon quantum dots, Nat. Commun. **10**, 1063 (2019).

[16] A. J. Sigillito, J. C. Loy, D. M. Zajac, M. J. Gullans, L. F. Edge, and J. R. Petta, Site-Selective Quantum Control in an Isotopically Enriched $^{28}Si/Si_{0.7}Ge_{0.3}$ Quadruple Quantum Dot, Phys. Rev. Appl. **11**, 061006 (2019).

[17] M. G. Borselli, R. S. Ross, A. A. Kiselev, E. T. Croke, K. S. Holabird, P. W. Deelman, L. D. Warren, I. Alvarado-Rodriguez, I. Milosavljevic, F. C. Ku, W. S. Wong, A. E. Schmitz, M. Sokolich, M. F. Gyure, and A. T. Hunter, Measurement of valley splitting in high-symmetry Si/SiGe quantum dots, Appl. Phys. Lett. **98**, 123118 (2011).

[18] Z. Shi, C. B. Simmons, J. R. Prance, J. King Gamble, M. Friesen, D. E. Savage, M. G. Lagally, S. N. Coppersmith, and M. A. Eriksson, Tunable singlet-triplet splitting in a few-electron Si/SiGe quantum dot, Appl. Phys. Lett. **99**, 233108 (2011).

[19] E. Kawakami, P. Scarlino, D. R. Ward, F. R. Braakman, D. E. Savage, M. G. Lagally, M. Friesen, S. N. Coppersmith,

M. A. Eriksson, and L. M. K. Vandersypen, Electrical control of a long-lived spin qubit in a Si/SiGe quantum dot, Nat. Nanotechnol. **9,** 666 (2014).

[20] P. Scarlino, E. Kawakami, T. Jullien, D. R. Ward, D. E. Savage, M. G. Lagally, M. Friesen, S. N. Coppersmith, M. A. Eriksson, and L. M. K. Vandersypen, Dressed photon-orbital states in a quantum dot: Intervalley spin resonance, Phys. Rev. B **95,** 165429 (2017).

[21] D. M. Zajac, T. M. Hazard, X. Mi, K. Wang, and J. R. Petta, A reconfigurable gate architecture for Si/SiGe quantum dots, Appl. Phys. Lett. **106,** 223507 (2015).

[22] X. Mi, C. G. Péterfalvi, G. Burkard, and J. R. Petta, High-Resolution Valley Spectroscopy of Si Quantum Dots, Phys. Rev. Lett. **119,** 176803 (2017).

[23] R. Ferdous, E. Kawakami, P. Scarlino, M. P. Nowak, D. R. Ward, D. E. Savage, M. G. Lagally, S. N. Coppersmith, M. Friesen, M. A. Eriksson, L. M. K. Vandersypen, and R. Rahman, Valley dependent anisotropic spin splitting in silicon quantum dots, npj Quantum Inf. **4,** 26 (2018).

[24] X. Mi, S. Kohler, and J. R. Petta, Landau-Zener interferometry of valley-orbit states in Si/SiGe double quantum dots, Phys. Rev. B **98,** 161404(R) (2018).

[25] F. Borjans, D. M. Zajac, T. M. Hazard, and J. R. Petta, Single-Spin Relaxation in a Synthetic Spin-Orbit Field, Phys. Rev. Appl. **11,** 044063 (2019).

[26] L. M. K. Vandersypen, H. Bluhm, J. S. Clarke, A. S. Dzurak, R. Ishihara, A. Morello, D. J. Reilly, L. R. Schreiber, and M. Veldhorst, Interfacing spin qubits in quantum dots and donors—hot, dense, and coherent, npj Quantum Inf. **3,** 34 (2017).

[27] C. H. Yang, A. Rossi, R. Ruskov, N. S. Lai, F. A. Mohiyaddin, S. Lee, C. Tahan, G. Klimeck, A. Morello, and A. S. Dzurak, Spin-valley lifetimes in a silicon quantum dot with tunable valley splitting, Nat. Commun. **4,** 2069 (2013).

[28] T. Ando, Valley splitting in the silicon inversion layer: Misorientation effects, Phys. Rev. B **19,** 3089 (1979).

[29] T. B. Boykin, G. Klimeck, M. A. Eriksson, M. Friesen, S. N. Coppersmith, P. von Allmen, F. Oyafuso, and S. Lee, Valley splitting in strained silicon quantum wells, Appl. Phys. Lett. **84,** 115 (2004).

[30] M. Friesen, M. A. Eriksson, and S. N. Coppersmith, Magnetic field dependence of valley splitting in realistic Si/SiGe quantum wells, Appl. Phys. Lett. **89,** 202106 (2006).

[31] M. Friesen, S. Chutia, C. Tahan, and S. N. Coppersmith, Valley splitting theory of SiGe/Si/SiGe quantum wells, Phys. Rev. B **75,** 115318 (2007).

[32] D. Culcer, X. Hu, and S. Das Sarma, Interface roughness, valley-orbit coupling, and valley manipulation in quantum dots, Phys. Rev. B **82,** 205315 (2010).

[33] G. Petersen, E. A. Hoffmann, D. Schuh, W. Wegscheider, G. Giedke, and S. Ludwig, Large Nuclear Spin Polarization in Gate-Defined Quantum Dots Using a Single-Domain Nanomagnet, Phys. Rev. Lett. **110,** 177602 (2013).

[34] P. Huang and X. Hu, Spin relaxation in a Si quantum dot due to spin-valley mixing, Phys. Rev. B **90,** 235315 (2014).

[35] A. L. Saraiva, M. J. Calderón, R. B. Capaz, X. Hu, S. Das Sarma, and B. Koiller, Intervalley coupling for interface-bound electrons in silicon: An effective mass study, Phys. Rev. B **84,** 155320 (2011).

[36] P. Huang and X. Hu, Electron spin relaxation due to charge noise, Phys. Rev. B **89,** 195302 (2014).

[37] L. Petit, J. M. Boter, H. G. J. Eenink, G. Droulers, M. L. V. Tagliaferri, R. Li, D. P. Franke, K. J. Singh, J. S. Clarke, R. N. Schouten, V. V. Dobrovitski, L. M. K. Vandersypen, and M. Veldhorst, Spin Lifetime and Charge Noise in hot Silicon Quantum dot Qubits, Phys. Rev. Lett. **121,** 076801 (2018).

[38] See Supplemental Material at http://link.aps.org/supplemental/10.1103/PhysRevApplied.13.034068 for measurement details, additional data, and modeling including Refs. [44–52].

[39] N. S. Lai, W. H. Lim, C. H. Yang, F. A. Zwanenburg, W. A. Coish, F. Qassemi, A. Morello, and A. S. Dzurak, Pauli spin blockade in a highly tunable silicon double quantum dot, Sci. Rep. **1,** 110 (2011).

[40] C. H. Yang, R. C. C. Leon, J. C. C. Hwang, A. Saraiva, T. Tanttu, W. Huang, J. C. Lemyre, K. W. Chan, K. Y. Tan, F. E. Hudson, K. M. Itoh, A. Morello, M. Pioro-Ladrière, A. Laucht, and A. S. Dzurak, Silicon quantum processor unit cell operation above one Kelvin, arXiv:1902.09126 (unpublished).

[41] J. M. Elzerman, R. Hanson, L. H. van Willems Beveren, B. Witkamp, L. M. K. Vandersypen, and L. P. Kouwenhoven, Single-shot read-out of an individual electron spin in a quantum dot, Nature **430,** 431 (2004).

[42] A. L. Saraiva, M. J. Calderón, X. Hu, S. Das Sarma, and B. Koiller, Physical mechanisms of interface-mediated intervalley coupling in Si, Phys. Rev. B **80,** 081305(R) (2009).

[43] T. Meunier, I. T. Vink, L. H. Willems van Beveren, K. J. Tielrooij, R. Hanson, F. H. L. Koppens, H. P. Tranitz, W. Wegscheider, L. P. Kouwenhoven, and L. M. K. Vandersypen, Experimental Signature of Phonon-Mediated Spin Relaxation in a Two-Electron Quantum dot, Phys. Rev. Lett. **98,** 126601 (2007).

[44] C. B. Simmons, J. R. Prance, B. J. Van Bael, T. S. Koh, Z. Shi, D. E. Savage, M. G. Lagally, R. Joynt, M. Friesen, S. N. Coppersmith, and M. A. Eriksson, Tunable Spin Loading and T_1 of a Silicon Spin Qubit Measured by Single-Shot Readout, Phys. Rev. Lett. **106,** 156804 (2011).

[45] V. N. Golovach, A. Khaetskii, and D. Loss, Phonon-Induced Decay of the Electron Spin in Quantum Dots, Phys. Rev. Lett. **93,** 016601 (2004).

[46] J. H. van Vleck, Paramagnetic relaxation times for titanium and chrome alum, Phys. Rev. **57,** 426 (1940).

[47] A. V. Khaetskii and Y. V. Nazarov, Spin-flip transitions between Zeeman sublevels in semiconductor quantum dots, Phys. Rev. B **64,** 125316 (2001).

[48] P. Y. Yu and M. Cardona, *Fundamentals of Semiconductors*, Graduate Texts in Physics (Springer, Berlin, Heidelberg, 2010).

[49] C. Tahan and R. Joynt, Relaxation of excited spin, orbital, and valley qubit states in ideal silicon quantum dots, Phys. Rev. B **89,** 075302 (2014).

[50] P. Boross, G. Széchenyi, D. Culcer, and A. Pályi, Control of valley dynamics in silicon quantum dots in the presence of an interface step, Phys. Rev. B **94,** 035438 (2016).

[51] U. Weiss, *Quantum Dissipative Systems* (World Scientific, Singapore, 2008), 3rd ed., Vol. 13.

[52] D. M. Pozar, *Microwave Engineering* (John Wiley & Sons, New Delhi, 2010), 3rd ed.

Correction: A conversion error rendered the presuperscript number 28 to Si incorrectly in the HTML format and has been fixed. The PDF version was processed correctly, without incident.